

Aerosol radiative effects in photosynthetically active radiation and total irradiance at a Mediterranean site from an 11-year database

Ismael L. Lozano^{1,2}, Guadalupe Sánchez-Hernández^{1,2}, Juan Luis Guerrero-Rascado^{1,2}, Inmaculada Alados^{1,3}, Inmaculada Foyo-Moreno^{1,2}

¹Andalusian Institute for Earth System Research, Granada, 18006, Spain

²Department of Applied Physics, University of Granada, Granada, 18071, Spain

³Applied Physics II Department, University of Málaga, Málaga, 29071, Spain

Corresponding author: ifoyo@ugr.es

<https://doi.org/10.1016/j.atmosres.2021.105538>

Abstract

This study addresses the analysis of the aerosol radiative forcing (ARF) and aerosol forcing efficiency (AFE) at surface in the Photosynthetically Active and Total radiation ranges in a Southwest Mediterranean site. A thorough analysis of a long-term database (2008-2018) has been performed, bringing very valuable results about both, the absolute values and trends in ARF and AFE for both spectral intervals. The largest monthly mean for aerosol optical depth at 500 nm (AOD_{500}) is found in summer (0.16 at July and August) meanwhile the lowest value is in winter (0.08 at November and December), with an interannual range varying from 0.11 ± 0.03 (in 2018) to 0.17 ± 0.03 (in 2014). The AFE variation range has been estimated between -12 and $-198 \text{ Wm}^{-2}\tau^{-1}$ for PAR and between -9 and $-450 \text{ Wm}^{-2}\tau^{-1}$ for Total irradiance. ARF varies between -1 Wm^{-2} and -23 Wm^{-2} in the PAR range, taking values from -1 to -40 Wm^{-2} in the Total one. This result points out the relevance of the aerosol effects on the PAR range, which can involve up to a 50% of the Total ARF. Moreover, a notable dependence of ARF and AFE on the solar position has been detected, increasing their absolute values at solar zenith angle

<https://doi.org/10.1016/j.atmosres.2021.105538>

from 0° to 45°-60° and decreasing to zero for lower solar positions. Additionally, this analysis has revealed the existence of a significant downward trend in AFE values for PAR, with a slope of $2.7 \text{ Wm}^{-2}\tau^{-1}\text{year}^{-1}$. Although the slope is positive, taking into account that the AFE values are negative, the slope value implies that the aerosol cooling radiative effect of aerosols is decreasing. However, no trends have been detected neither in AFE nor ARF values in the Total solar range. These results evidence the long-term aerosol effects over the different spectral intervals and emphasize the need for detailed analysis of the aerosol radiative effects on fundamental spectral intervals such as the PAR range.

Keywords: Aerosols; Photosynthetically active radiation; Radiative forcing.

1.- INTRODUCTION

Photosynthetically Active Radiation (PAR) is commonly defined as the electromagnetic radiation in the waveband between 400 and 700 nm (McCree, 1972). This spectral interval, which contains the maximum of the solar radiation spectrum, plays a fundamental role in vegetation productivity and agricultural research (Caya et al., 2018; McCree, 1981). PAR is the driver of the photosynthesis process and the biochemical reactions involved in it (Wu et al., 2019) and, therefore, the beginning of the plant growth. Moreover, PAR is a key factor controlling ecological processes such as the terrestrial carbon and hydrological cycles (Jonard et al., 2020; Potter et al., 2007, 2008). Along its path throughout the atmosphere, solar radiation, and particularly PAR, is attenuated by scattering and absorbing processes, being atmospheric aerosols, the main

factor determining the amount and distribution of solar radiation reaching the Earth's surface in absence of clouds. Aerosol particles affect the Earth's radiation budget both directly, by scattering and absorption, and indirectly, modifying cloud properties (e. g. Eswaran et al., 2019; Farahat et al., 2016; Satheesh & Krishna Moorthy, 2005). Aerosol attenuation presents an important spectral dependence. Thus, while spectral aerosol absorption decreases with wavelength, aerosol scattering efficiency strongly depends on the aerosol composition, increasing with wavelength for mineral dust and decreasing in case of urban pollution (Bergstrom et al., 2007). Due to this spectral dependence of the attenuation processes, aerosol effects over shorter wavelengths, such as the PAR interval, take a special relevance (Xu et al., 2003).

In order to quantify the radiative balance variations due to changes in atmospheric aerosols, the concepts of aerosol radiative forcing (ARF) and aerosol forcing efficiency (AFE) are widely employed. ARF is defined as the change in the net radiation due to variations in the atmospheric aerosol properties with respect to an aerosol-free atmosphere. ARF highly depends on the aerosol size distribution and composition (e.g. Foyo-Moreno et al., 2014). Thus, while mineral dust particles show negative ARF values associated to a strong cooling, the anthropogenic aerosols exhibit a complex behavior, with positive and negative ARF values depending on many factors such as greenhouse gases and surface changes (e.g. Andreae et al., 2005; Charlson et al., 1991; Esteve et al., 2012; Gopal et al., 2014; Hansen et al., 2011; Satheesh & Krishna Moorthy, 2005; Zhuang et al., 2013). On the other hand, AFE is defined as the rate at which the atmosphere is forced per unit of aerosol optical depth, allowing for a more detailed assessment of the radiative forcing considering the aerosol type.

Several studies have analyzed the impact of different aerosol types, and particularly their ARF, on total solar radiation (280-3000 nm) worldwide (e.g. Sicard et al., 2016; Sorribas et al., 2019; Zhang et al., 2018). However, aerosol radiative effects and its relationship to climate change remain inaccurate (IPCC 2013; Stocker et al., 2013). This uncertainty is larger in the PAR range because of the scarcity of related studies (Lyamani et al., 2006a; Mateos et al., 2014; Zhu et al., 2015). In fact, a worldwide routine network for the measurement of PAR is not yet established and PAR is often calculated as a constant ratio of the Total irradiance (Alados et al., 1996; Ge et al., 2011). Thus, one of the main drawbacks for this type of analysis is the lack of simultaneous and reliable measurements of PAR and aerosol properties. This limitation is stronger when the analysis is focused on trends in long-term databases and on the Mediterranean region (Di Biagio et al., 2009).

Recently, Obregón et al. (2020) studied the spatial and temporal AOD variations and the effects on solar radiation at the surface in the Mediterranean basin during a long period (2000–2018). Previously, they quantified ARF and AFE at Évora (Portugal, Southwestern Iberian Peninsula) during thirteen years (Obregón et al., 2017). In this Mediterranean region, temperature is increasing faster than the world average during the last decades (Lionello et al., 2014), and climate projections predict an increase of extreme climatic events, such as heat waves and droughts (Garcia-Herrera et al., 2014; Lionello et al., 2014). Besides, the Mediterranean region is subject to high aerosol loads, especially during spring and summer (Nabat et al., 2015), leading this region as a benchmark for climatic effect studies.

In this context, this aims to assess the aerosol radiative effects at surface on PAR for an urban middle-latitude site (Granada) in the Mediterranean basin for the decade 2008-2018. Local aerosols sources are traffic, local mineral dust during the dry season, and anthropogenic aerosols in winter from fuel oil combustion for domestic heating (Titos et al., 2012, 2017). At the same time, this site is also frequently influenced by emissions of several allochthonous aerosols sources such as continental aerosols from Europe and mineral dust from Africa (Fernández et al., 2019; Guerrero-Rascado et al., 2008, 2009; Lyamani et al., 2006a, 2006b, 2010), transported smoke from North America, North Africa and Europe (Alados-Arboledas et al., 2011; Baars et al., 2019; Ortiz-Amezcu et al., 2014; 2017; Titos et al., 2017), extraordinarily, aerosols events from volcanic plumes (Navas-Guzmán et al., 2013; Sicard et al., 2012), and oceanic aerosols from Arctic and Atlantic oceans or maritime aerosols from the Mediterranean sea (Cariñanos et al., 2021; Pérez-Ramírez et al., 2016). Due to this variety in aerosol sources and types, aerosols over Granada are complex and variable making this an attractive region for the analysis of the aerosol radiative effects.

To this aim, AFE and ARF values for the PAR and Total ranges for cloud-free situations have been estimated, and analyzed in detail for different years and solar positions. Additionally, potential AFE and ARF trends at both spectral ranges, PAR and Total, have been assessed and compared.

2.- EXPERIMENTAL SITE AND DATASET

Measurements used in this study have been collected at the radiometric station installed on the roof of the IISTA-CEAMA building at Granada (37.16 °N, 3.61 °W, 680 m.a.s.l.), an urban site located in the Southeast of Spain in the West Mediterranean region. This radiometric station is managed by the Atmospheric Physic Research Group (GFAT) at the University of Granada and is part of the observatory AGORA (Andalusian Global ObservatoRy of the Atmosphere) in the framework of ACTRIS (Aerosol, Clouds and Trace Gases Research Infrastructure). The period analyzed encompasses the decade 2008-2018. Granada presents large seasonal temperature differences, characterized by cool winters and hot summers, with mean daily maximum temperature at surface of $(14.6 \pm 2.4) ^\circ\text{C}$ in winter and $(32 \pm 3) ^\circ\text{C}$ for 1981-2010 period (AEMET, Spanish Meteorology Statal Agency).

In this study, one-minute measurements of Photosynthetically Active Radiation (PAR) were measured with a SKP 215 PAR Quantum Sensor (#28715) manufactured by Skye Instruments. This instrument measures the solar radiation in the range of 400-700 nm using a blue enhanced planar diffused silicon detector with a sensitivity of $0.015 \mu\text{A}/\mu\text{mol m}^{-2}\text{s}^{-1}$. The quantum sensor has a maximum relative error <5%. Simultaneous one-minute measurements of total solar irradiance were recorded with a radiometer CM11 (#861452) manufactured by Kipp&Zonen. This instrument measures broadband solar irradiance in the range of 280-2800 nm and complies with International Organization for Standardization (ISO) 9060 criteria for an ISO secondary standard pyranometer. Both measurements were recorded in a CR10X data logger manufactured by Campbell Scientific.

136 Additionally, Aerosol Optical Depth (AOD) values, measured every 15 minutes by a
137 CIMEL Sun/sky photometer (CE-318-4) were used in this study. This instrument, which
138 is integrated in the AERONET network (Holben et al., 1998), measures direct solar
139 irradiance with a 1.2° full field of view at 340, 380, 440, 500, 675, 870, 940 and 1020 nm
140 as well as sky radiances in the almucantar and principal plane geometries at 440, 675,
141 870 and 1020 nm. All radiance measurements are processed following the AERONET
142 protocol as described by Holben et al. (1998), obtaining columnar aerosol properties at
143 different quality levels (1.0, 1.5, 2.0). Version 3 of AOD at level 2.0 (Giles et al., 2019),
144 the highest quality AERONET data, was used in this study, except for 2014 for which only
145 version 2 at 2.0 level AOD was available. AOD data has a total uncertainty of 0.01 for
146 wavelengths ≥ 440 nm and 0.02 for shorter wavelengths (Holben et al., 1998). Sun-
147 photometer also provided the surface albedo measurements used in this study at 440,
148 675, 870 and 1020 nm with a total uncertainty of 0.02 (Foyo-Moreno et al., 2014). Both,
149 CIMEL photometer and radiometers involved in this study have been intercompared
150 respect to reference instruments several times along the 11-year period analyzed, with
151 their last intercomparison dated on May 2020 for the CIMEL photometer, May 2019 for
152 the CM11 pyranometer and August 2020 for the PAR sensor. CIMEL were calibrated
153 following AERONET protocols (Holben et al., 1998) at the RIMA calibration facilities at
154 Valladolid, Spain, while the radiometers have been intercompared with a Kipp&Zonen
155 CMP21 and a LICOR-190SA, respectively, following WMO procedure for intercomparison
156 (WMO, 2008). Particularly, the calibration factors applied in this study showed a change
157 of 0.15 mV/Wm^{-2} , in CM11 pyranometer, and 0.4 mV/Wm^{-2} , in PAR sensor, for the entire
158 period 2008-2018. This involves an annual average change of $0.013 \text{ mV/Wm}^{-2} \text{ year}^{-1}$ and
159 $0.027 \text{ mV/Wm}^{-2} \text{ year}^{-1}$ for Total and PAR irradiance sensor, respectively. Both values are

notably below the maximum change per year (long-term stability) detailed by the corresponding manufacturer, 0.5% for the CM11 and 2% for SKP 215 PAR Quantum Sensor, ensuring the calibration factor stability required for a trend analysis.

3.- METHODOLOGY

3.1 Data analysis and selection of cloud-free scenarios

To perform the analysis of the aerosol radiative effects, a database of simultaneous measurements of PAR, Total irradiance and AOD has been built for the period 2008-2018. This vast database ensures a large variety of seasonal processes, solar geometries and meteorological conditions and guarantees the representativeness of the dataset for the analysis proposed here.

A deep quality control has been applied to this final dataset in order to detect and eliminate potential erroneous measurements. First, only those measurements recorded for solar zenith angles smaller than 80° have been selected to avoid solar radiation data affected by a cosine response error, the maximum difference from the ideal response for PAR Quantum Sensor was approximately 7% at a zenith angle of 80° (Akitsu et al., 2017). Additionally, those cases in which total global irradiance reached higher values than extraterrestrial total irradiance ($k_t > 1$) or diffuse irradiance higher than global irradiance ($k_d > 1$) were removed. Outliers were detected by visual inspection and consequently removed. Possible troubles associated with power supply and temperature of the acquisition system were also checked.

Additionally, a thorough analysis of the AOD values along the period of study has been performed. Thus, data has been monthly grouped along the entire period in order to analyze seasonal evolution and a detailed statistical has been computed including arithmetic mean (Ave), standard deviation (SD), median (Md), minimum (Min), maximum (Max), percentiles 5th, 25th, 75th and 95th (P5, P25, P75 and P95, respectively), skewness (Ske), kurtosis (Kur) and the variation coefficient (VC) defined as the ratio between SD and the arithmetic mean.

In order to only account for aerosol effects, cloud-free situations have been selected applying the criterion proposed by Alados-Arboledas et al. (2000). This criterion detects as cloud-free situations those in which:

$$k_t > 0.53 + 0.31 \cos \text{SZA} - 0.15 \cos^2 \text{SZA} \quad (1)$$

where k_t is the clearness index, defined as the ratio between the total irradiance ground-measured and the extraterrestrial total irradiance ($G_{\text{ext}} = E_o I_{\text{sc}} \cos \text{SZA}$), both on a horizontal plane, where SZA is the solar zenith angle, E_o is the eccentricity correction factor and the value used of the Solar Constant (I_{sc}) is 1367 Wm^{-2} (Iqbal, 1983). The variability of the Solar Constant on the 11-year solar cycle has not been considered in this study. This empirical criterion, based on coefficients derived from a fitting to a polynomial function has been explicitly developed for Granada. This criterion only requires global irradiance measurements, commonly available at most radiometric stations.

3.2 AFE and ARF estimation

The ARF is defined as the difference between the measured net irradiance (F_{net}) and the same magnitude for an aerosol-free atmosphere ($F_{net,a}$):

$$ARF = F_{net} - F_{net,a} \quad (2)$$

where F_{net} is the difference between the downward and the upward irradiances at the Earth's surface. Net irradiances under the presence/absence of aerosols can be written, respectively, as:

$$F_{net} = (1 - A)I \quad (3)$$

$$F_{net,a} = (1 - A)I_a \quad (4)$$

where I is the experimental irradiance, I_a is the estimated irradiance under absence of aerosols, and A is the surface albedo.

The aerosol forcing efficiency (AFE) is defined as the change in ARF per unit increase in AOD for a certain wavelength (Bush and Valero, 2003):

$$AFE = \frac{dARF}{dAOD} \quad (5)$$

Thus, AFE at surface can be computed from the slope of the linear regression between ARF and AOD at fixed SZA (Antón et al., 2011; Díaz et al., 2007; García et al., 2006).

Different methodologies to estimate ARF have been proposed in literature. An extended method involves the use of radiative transfer models to estimate the net irradiance fluxes (Eswaran et al., 2019; Mateos et al., 2014; Sivan & Manoj, 2019). However, this procedure involves relevant assumptions such as the atmospheric composition and the aerosol layer description, which could lead to important errors. In this study, the so-

called direct method proposed by Satheesh and Ramanathan (2000) has been used.

Once cloud-free situations have been selected from the database, AFE is derived as the

slope of the linear fit between the experimental F_{net} values and AOD at fixed SZA:

$$AFE = \frac{dF_{net}}{dAOD} \quad (6)$$

Then, ARF at surface is obtained as a result of multiplying AFE by the annual AOD average at the corresponding solar position (Di Biagio et al., 2010; Foyo-Moreno et al., 2014).

The advantage of this method is that AFE is directly computed from the experimental data without further assumptions on the radiative fluxes under aerosol-free conditions.

This method shows an important dependence on the solar zenith angle and, therefore, its application and analysis is limited to specific solar zenith intervals.

Particularly, AOD values at 500 nm have been used to analyze the aerosol effects on the PAR for roughly being the central wavelength in this spectral range. On the other hand, AOD at 675 nm has been chosen to estimate AFE and ARF for the Total irradiance considering that the central wavelength of the solar spectrum is roughly 680 nm (Di Biagio et al., 2010). This decision is also supported by previous works (e.g. Foyo-Moreno et al., 2014; Li et al., 2020; Romano et al., 2016).

Additionally, five categories of solar zenith angles to compute both AFE and ARF, namely 15°, 30°, 45°, 60° and 75° ($\pm 1^\circ$), have been considered, in order to cover the majority of solar positions. Moreover, surface albedo provided by AERONET at 675 nm for our station has been used. Annual average surface albedo was estimated and employed in the calculation of the ARF, being 0.14 the annual average for all years, except for 2009

and 2013 for which a value of 0.15 was found. The overall error in next flux increases by less than 0.3% due to the uncertainty in surface albedo (Di Biagio et al., 2010).

3.3 Trend analysis

Finally, the non-parametric Mann-Kendall test (Mann, 1945) has been applied to detect time series trends for AOD, ARF and AFE with statistical significance. In addition, the Sen estimation of the trend slope has been performed, which complements the Mann-Kendall test (Sen, 1968). The use of the Sen method is appropriate for evaluating trends in time series as it is not affected by outliers and gaps, making it a common method in literature (e.g. Buffoni et al., 1999; Da Silva et al., 2010; Dadashi-Roudbari and Ahmadi, 2020; Kodera et al., 2008; Kuo et al., 2020; Olmo & Alados-Arboledas, 1995; Zou et al., 2016). To perform these calculations the kbttau.m software developed by Jeff Burkey (*Mann-Kendall Tau-b with Sen's Method (Enhanced)*, 2020) was used.

4.- RESULTS AND DISCUSSION

4.1 AOD characterization

First, to have a brief global view, a general characterization of the whole databases including all variables analysed has been included in Figure 1, showing the monthly averages for every year. The two data series for the solar irradiance measurements display the same typical annual cycle with summer maximum (for example, (730 ± 60) Wm^{-2} for Total and (340 ± 30) Wm^{-2} for PAR in July 2016) and winter minimum, driven by the annual course of the solar zenith angle, with interannual variability.

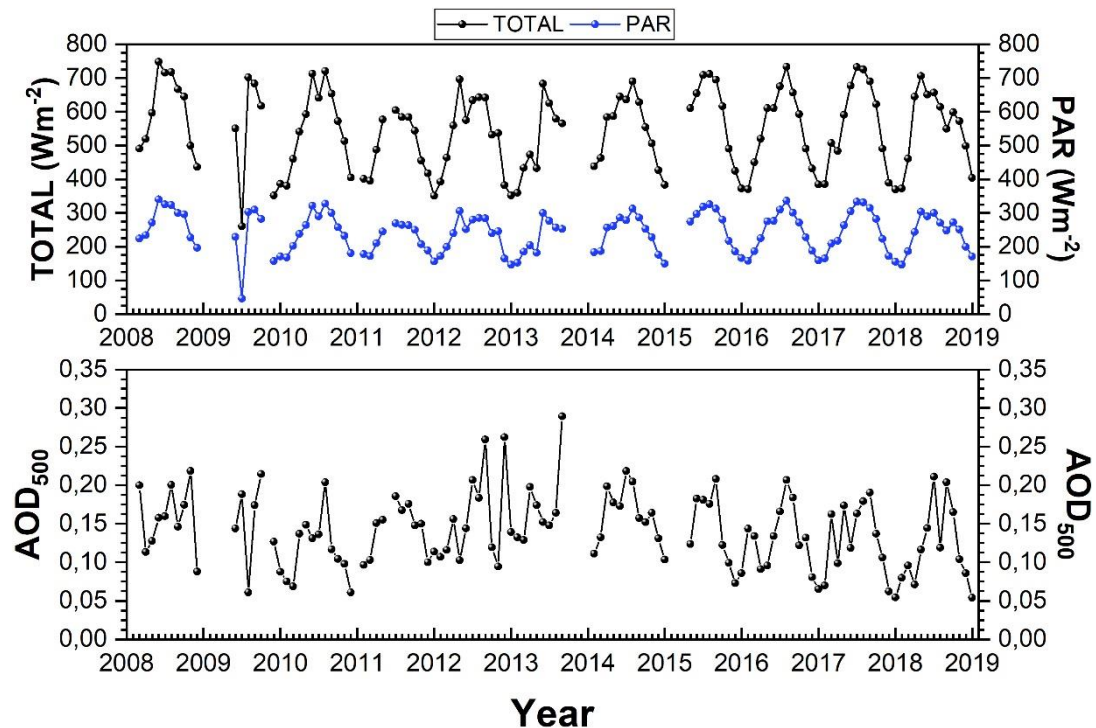


Figure 1. Time series of monthly mean PAR (black line), Total (blue line) and AOD at $\lambda = 500\text{nm}$ (AOD_{500}), for 2008-2018 years.

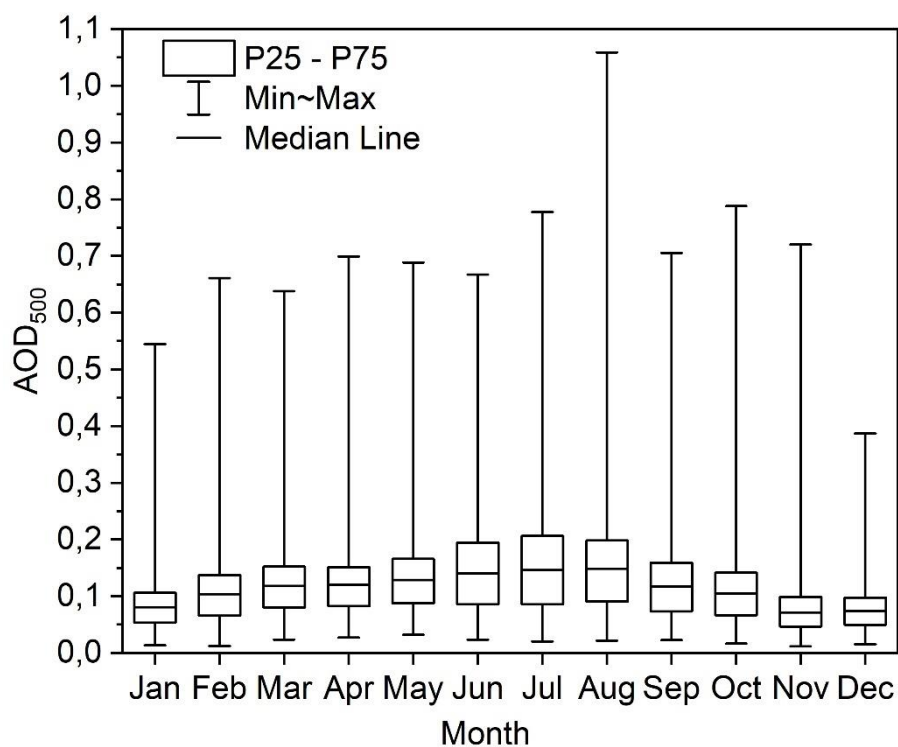
Focusing on AOD, for the sake of clarity, the analysis of AOD is presented here based on 500 nm (Table 1 and Figure 2). The largest monthly mean AOD_{500} is found in summer (0.16 at July and August) meanwhile the lowest values are in winter (0.08 at November and December). The maximum/minimum values occur, respectively, in summertime due to the higher frequency Saharan dust outbreaks (Salvador et al., 2014), and in wintertime due to the low probability of these events (Gkikas et al., 2013, 2018; Querol et al., 2009) over the Mediterranean region. This behaviour agrees with previous studies. Mateos et al. (2014) reported a minimum and maximum AOD_{440} in November and July, respectively, at the same location during the period 2004-2012. Antón et al. (2011) found minimum AOD_{380} (0.14 ± 0.05) and AOD_{400} (0.12 ± 0.05) in November and

December, respectively, coinciding in time with our minimum AODs, but differing with respect to maximum values found in May (0.26 ± 0.12 for AOD₃₈₀ and 0.24 ± 0.12 for AOD₄₄₀). These differences might be caused by the short period used (2006-2008), probably limiting its representativeness. In a later study, Mateos et al. (2015) studied the aerosol load over the Iberian Peninsula in five geographical sectors and they found values for AOD₄₄₀ varying between 0.15 and 0.20. This annual cycle is also found by Bennouna et al. (2016) for long measurement records (2003-2014) obtained at two sites of Spain located in the North Central region, with values for AOD₄₄₀ of 0.16 ± 0.09 in June and 0.08 ± 0.06 in December. Segura et al. (2017) found a mean value of 0.15 ± 0.11 for AOD₅₅₀ with the same seasonal pattern for a site located Mediterranean coastal area in Spain during the period 2007-2016. Sicard et al. (2016) also found for AOD₄₄₀ a clear annual cycle (maxima of 0.22 at Erba and 0.27 at Palma observed in July) for a 5-year period for different locations in the Western Mediterranean Basin.

Table 1. Monthly statistics of AOD₅₀₀ for the period 2008-2018 based on daily values: Number of datapoints (N), Average (Ave), Standard deviation (SD), Median (Md), Percentiles (P5, P25, P75, P95), Skewness (Ske), Kurtosis (Kur) and coefficient of variation (CV).

Month	N	Ave	Md	P5	P25	P75	P95	Ske	kur	CV(%)
January	3603	0.09±0.06	0.08	0.03	0.06	0.11	0.20	2.19	10.92	63
February	3840	0.11±0.06	0.10	0.04	0.07	0.14	0.21	1.73	9.51	54
March	4641	0.13±0.07	0.11	0.05	0.08	0.16	0.26	1.89	9.20	54
April	5158	0.13±0.07	0.12	0.05	0.08	0.16	0.25	2.20	11.36	54
May	6986	0.13±0.07	0.13	0.06	0.09	0.17	0.25	2.17	12.12	51
June	10344	0.15±0.09	0.14	0.05	0.09	0.21	0.34	1.50	5.65	60
July	13132	0.16±0.09	0.15	0.05	0.09	0.22	0.34	1.20	4.61	58
August	10763	0.16±0.09	0.15	0.05	0.10	0.22	0.34	1.39	6.73	58
September	8447	0.13±0.07	0.12	0.05	0.08	0.17	0.26	1.35	5.43	55
October	6529	0.11±0.06	0.10	0.04	0.07	0.15	0.24	1.51	7.57	56
November	4771	0.08±0.05	0.07	0.03	0.05	0.10	0.16	2.90	20.63	63
December	3436	0.08±0.04	0.07	0.03	0.05	0.10	0.16	1.68	7.67	53

296 The analysis of P5 and P95 is similar to the trend of the average values. The median AOD
 297 values are smaller than the mean, what is a common feature over the Iberian regions
 298 (Mateos et al., 2015). The absolute difference between the median and third quartile is
 299 also larger than the absolute difference between the median and the first quartile
 300 except at two months, namely April and May. This last result is also in accordance with
 301 those found by Mateos et al. (2015). The kurtosis and asymmetry data for AOD show
 302 that the distribution for all months is leptokurtic and positive asymmetric, obtaining the
 303 highest asymmetry values for November, while the lowest values are found in July.



304

305 Figure 2. Monthly statistics of AOD₅₀₀ for the period 2008-2018. Bars correspond to the
 306 minimum and maximum values, the box limits are the P25 and P75 percentiles and the midline
 307 is the median.

The box-whisker diagram plot in Figure 2 showed a clear seasonality (already observed in Table 1) with higher values in central months, with a high standard deviation specially at August due to African dust intrusions additionally to resuspension processes of local mineral aerosols owing to the dryness of the soil. Thus, the maximum AODs were found in summer and minimum values in winter. This evident AOD annual pattern is also found at seven sites in the Iberian Peninsula covering different aerosol types and environmental conditions during three coincident years (2010-2012) (Foyo-Moreno et al., 2019). The interquartile range P75-P25 is also larger in summer. It is worthy to note relatively high values of maximum AOD₅₀₀ (0.66) and its P95 (0.21) in February. Despite of the low frequency of Saharan dust events over the Mediterranean region in winter (Gkikas et al., 2013, 2018; Querol et al., 2009), this is explained due to the intense Saharan dust events occurring in February 2016 and 2017 (Cazorla et al., 2017; Fernández et al., 2019), and also the increase in the anthropogenic local emissions in winter in addition to the orographic and meteorological conditions of Granada which favors the particle stagnation (Lyamani et al., 2012).

To study the interannual variability the box-wisher diagram plot of AOD₅₀₀ at Granada is shown in Figure 3, for 2008-2018 years. The interannual range of AOD₅₀₀ varies from 0.11 ± 0.08 in 2018 to 0.16 ± 0.14 in 2014 for, and showed firstly a decreasing trend in the subperiod 2008-2010, an increasing trend in 2010-2014 and a latter decreasing trend from 2014, but the Mann Kendall test revealed a slope of -0.001 with a p-value of 0.53 and, therefore, with no trend for AOD₅₀₀. The years with higher variability are 2012, 2015 and 2016, with a maximum difference between the extreme values for 2012. In general, a clear decrease in the aerosol load over the Iberian Peninsula has been observed since

the 2000s. In particular, Mateos et al., 2015 found a decrease of -0.07 per decade in AOD₄₀₀ for the Southeastern sector. Li et al. (2014) found a decreasing trend for a large stations number around the world (including Granada). Thus, the largest decreases were found over western Europe, reaching -0.1 per decade, and particularly they found at Granada a slope of -0.03 per decade for AOD₄₀₀. In our study, no significant trend has been found for AOD₅₀₀ in the whole data.

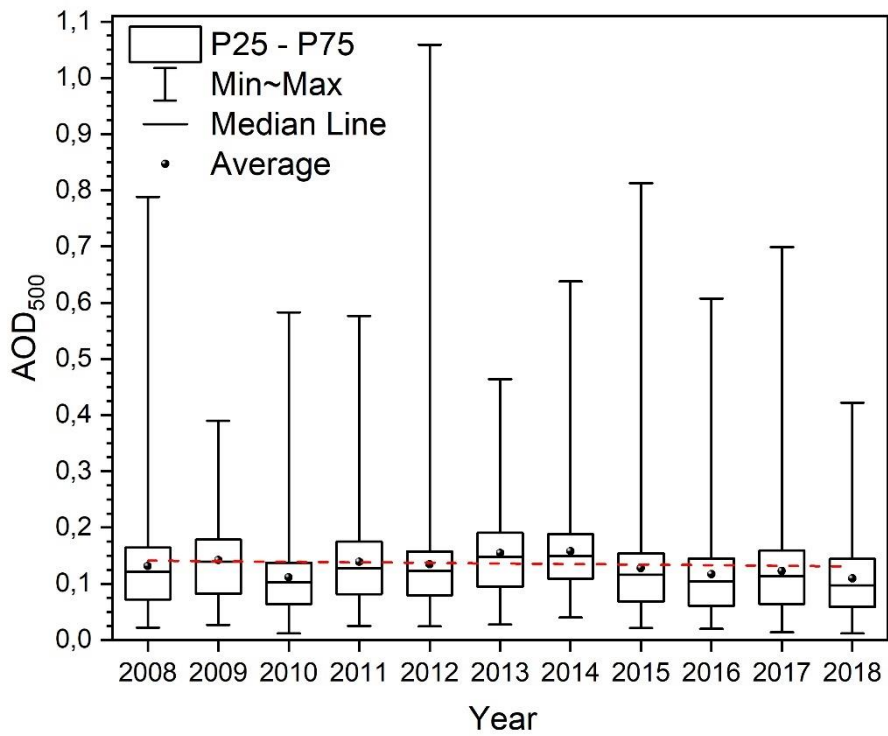


Figure 3. Annual statistics of AOD₅₀₀ for the period 2008-2018. Bars correspond to the minimum and maximum values, the box limits are the P25 and P75 percentiles, the midline is the median and the sphere is the mean value. Dashed lines point out the linear trend evaluated by the Sen method.

4.2 Analysis of AFE and ARF

Figure 4 shows the relationship between PAR and AOD₅₀₀ for the entire studied period at different solar zenith angles centered at 15°, 30°, 45°, 60° and 75° (± 1°). For each year, five well-differentiated point clouds are observed, corresponding each of them to one of the five solar positions analyzed. As it was expected, the $F_{\text{net}}^{\text{PAR}}$ increases for lower solar zenith angles due to the lower solar radiation path through the atmosphere at this solar position, increasing the solar irradiance reaching the surface. Additionally, a larger spread of the datapoints is observed for low values of AOD because of the large influence of the measurement uncertainty on the low AOD values. A similar behaviour has been observed for AFE^{total} (not shown here). An additional explanation of this datapoint large spread can be the existence of numerous sources of aerosols, which gives this region a high variability and complexity (Benavent-Oltra et al., 2017; Bravo-Aranda et al., 2015; Cazorla et al., 2017; Córdoba-Jabonero et al., 2011; Pérez-Ramírez et al., 2016).

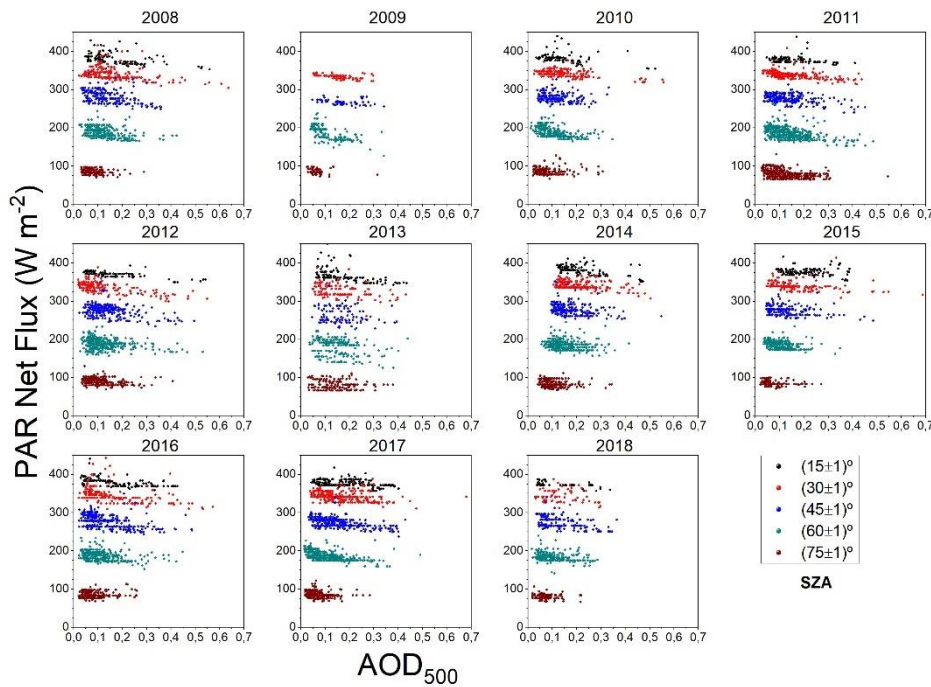


Figure 4. Evolution of PAR Net Flux versus AOD₅₀₀ for the period 2008-2018.

As it was described in Section 3.2, the slope of the linear fit at each angle category in Figure 4 represents the AFE. Both, AFE^{PAR} and AFE^{total} present negative values (Table 2), leading to a cooling effect by aerosols over Granada (Granados-Muñoz et al., 2019). AFE^{PAR} varies between -12 and -198 Wm⁻²τ⁻¹ while AFE^{total} ranges between -9 and -450 Wm⁻²τ⁻¹, showing a higher variability than in the PAR interval. These results agree with previous studies. Thus, Di Biagio et al. (2010) accounted for an AFE^{total} value of -309 ± 16 Wm⁻²τ⁻¹ for solar zenith angles between 15° and 25° and mixed aerosols at Lampedusa (Italy). Lower values have been estimated for other aerosol types as desert mineral dust and urban/industrial and biomass burning aerosols (Di Biagio et al., 2010). In this study, AFE^{PAR} entails between 20 and 60 % of the AFE^{total} with an average value of 30% for the whole dataset, which points out the relevance of the aerosol effects on PAR and the influence of this spectral interval.

Table 2. Surface aerosol forcing efficiency (Wm⁻²τ⁻¹) for PAR and Total irradiance (ARE^{PAR} and ARE^{total}, respectively) with its variability at one standard deviation level by years for different solar zenith angles (SZA).

Year	AFE ^{PAR} (Wm ⁻² τ ⁻¹)				
	SZA (°)				
	15	30	45	60	75
2008	-65±12	-71±10	-103±14	-83±11	-28±11
2009		-47±8	-37±13	-198±18	-35±23
2010	-49±15	-52±5	-52±15	-117±12	1±11
2011	-27±13	-55±6	-75±8	-101±7	-49±6
2012	-43±4	-76±7	-80±10	-51±8	-36±8
2013	-92±15	-76±17	-50±30	-90±20	-27±13
2014	-78±10	-49±7	-69±12	-40±10	-17±9
2015	-18±9	-33±8	-53±11	-85±10	-12±9
2016	-64±8	-82±11	-94±9	-34±8	32±8

2017	-27±5	-40±6	-74±5	-96±5	-40±8
2018	-42±1	-40±30	-83±13	-56±10	-24±14
AFE ^{total} (Wm ⁻² τ ⁻¹)					
SZ A (°)					
Year	15	30	45	60	75
2008	-170±30	-183±23	-300±30	-220±30	-30±40
2009		-220±30	-155±4	-450±50	-90±60
2010	-150±37	-144±17	-210±40	-330±40	-70±30
2011	-192±34	-168±18	-199±22	-281±19	-116±16
2012	-114±13	-163±18	-180±30	-123±19	-70±20
2013	-270±50	-200±50	-120±70	-220±60	-60±40
2014	-128±22	-126±23	-210±40	-210±30	-9±24
2015	-84±23	-92±18	-150±30	-310±30	-50±30
2016	-203±21	-200±30	-240±21	-205±23	59±21
2017	-149±13	-156±15	-219±12	-374±15	-170±30
2018	-170±19	-190±70	-310±40	-400±40	-120±60

Regarding the AFE dependence on solar zenith angle, both AFE^{PAR} and AFE^{total} showed enhanced values at roughly 45° or 60°. Other authors have reported a different pattern of this dependence with relatively constant or opposite trend for lower values of SZ A and the same decreasing trend obtained in this work for high SZ A values. Thus, Di Biagio et al. (2009) pointed out that this trend depends on the aerosol type and seems to be reversed for urban/industrial-biomass burning aerosols. Additionally, several authors suggested that the inflection point in this trend depends on the aerosol properties (Di Biagio et al., 2009, 2010; Formenti et al., 2002). This dependence of AFE on SZ A can be explained by the combination of different factors. As the solar radiation path increases in the atmosphere, the attenuation as well as the diffuse fraction increases, especially at shorter wavelengths. On the other hand, for high SZ A, the atmosphere is optically thicker and the AFE tends to decrease. Consequently, the AFE displays a dependence on SZ A, which confirms the need to estimate forcing efficiency at fixed solar position applying the direct method employed in this study (Di Biagio et al., 2009, 2010; Formenti et al., 2002; Meloni et al., 2005; Nemesure et al., 1995).

The same analysis has been carried out for the ARF. Table 3 shows the values for ARF^{PAR} and ARF^{total} during the full period, ranging from -1 to -23 Wm^{-2} and from -1 to -40 Wm^{-2} for ARF^{PAR} and ARF^{total} , respectively. These values are in accordance to those reported by other authors. Thus, Meloni et al. (2005) found ARF^{PAR} values between -10 and -20 Wm^{-2} at Lampedusa. Our work has reported a percentual ratio ARF^{PAR}/ARF^{total} of 50% in average, that is a higher value than the one found for AFE (30%). This average percentage found for ARF is higher than the mean value obtained at Granada for the ratio PAR to Total (43%) with values varying between 33 and 52% (Foyo-Moreno et al., 2017), highlighting the important role of the aerosols on PAR, greater than on Total. Following Ma et al. (2007), the ratio PAR to Total irradiance for various locations around the world present values between 35 and 58%.

Table 3. Surface aerosol radiative forcing (Wm^{-2}) for PAR and Total irradiance (ARF^{PAR} and ARF^{total} , respectively) with its variability at one standard deviation level by years for different solar zenith angles (SZA).

Year	$ARF^{PAR}(Wm^{-2})$				
	SZA ($^{\circ}$)				
	15	30	45	60	75
2008	-11 \pm 9	-12 \pm 9	-15 \pm 10	-10 \pm 7	-2 \pm 2
2009	-	-8 \pm 4	-6 \pm 5	-23 \pm 14	-3 \pm 3
2010	-7 \pm 7	-8 \pm 6	-6 \pm 5	-13 \pm 8	0 \pm 1
2011	-5 \pm 4	-9 \pm 6	-10 \pm 7	-13 \pm 9	-6 \pm 4
2012	-6 \pm 5	-12 \pm 10	-11 \pm 8	-6 \pm 5	-4 \pm 3
2013	-15 \pm 11	-12 \pm 9	-9 \pm 8	-13 \pm 9	-4 \pm 4
2014	-17 \pm 8	-10 \pm 5	-12 \pm 6	-6 \pm 4	-2 \pm 2
2015	-4 \pm 3	-6 \pm 5	-7 \pm 6	-9 \pm 5	-1 \pm 1
2016	-11 \pm 8	-14 \pm 11	-12 \pm 9	-3 \pm 3	3 \pm 2
2017	-4 \pm 3	-7 \pm 4	-11 \pm 7	-10 \pm 7	-3 \pm 2
2018	-6 \pm 4	-5 \pm 6	-11 \pm 8	-6 \pm 4	-2 \pm 2
Year	$ARF^{total}(Wm^{-2})$				
	SZA ($^{\circ}$)				
	15	30	45	60	75
2008	-21 \pm 19	-23 \pm 20	-31 \pm 25	-19 \pm 14	-2 \pm 3
2009	-	-26 \pm 13	-20 \pm 9	-40 \pm 30	-4 \pm 5

2010	-15±17	-15±15	-18±14	-25±18	-4±4
2011	-24±20	-21±17	-20±17	-26±20	-9±7
2012	-14±14	-22±21	-19±17	-11±10	-5±5
2013	-30±30	-25±22	-15±17	-24±20	-6±7
2014	-21±13	-20±13	-27±16	-23±13	-1±2
2015	-12±10	-12±13	-14±13	-21±14	-2±3
2016	-28±24	-30±30	-24±22	-15±13	3±4
2017	-18±13	-20±14	-24±17	-27±22	-7±5
2018	-16±14	-18±19	-30±24	-30±30	-5±6

406

407 Regarding the dependence of ARF on solar position, a similar pattern to that of AFE is
408 found. The absolute ARF values increase with increasing SZA up to 45° or 60°, depending
409 on the year considered, and then decrease. However, this dependence is less
410 pronounced than for AFE, with values relatively constant for SZA below an intermediate
411 value. The value of SZA for the change always is coinciding with the values obtained for
412 AFE and also is coinciding for PAR and Total irradiance except for 2018. This trend is
413 similar to that obtained by Meloni et al. (2005), but the trend is reversed for aerosols
414 more absorbing. This fact may explain the different behavior below a given SZA value.
415 Our work covers a long period including a wide variety of aerosols and, thus, this mixture
416 generally exhibits large values of single scattering albedo. In fact, the maximum values
417 of single scattering albedo registered at Granada during the years 2010-2012 are close
418 to 1, which indicates that Granada recorded events of non-absorbing aerosols (Foyo-
419 Moreno et al., 2019).

420 Comparing our results with previous studies, we found similar values of both AFE and
421 ARF for both PAR and Total irradiance. Antón et al. (2012) performed ARF and AFE
422 calculations at Granada for Total irradiance with another method and they found, values
423 of ARF between -100 and -200 Wm⁻² and AFE of -115 Wm⁻²τ⁻¹ at 675 nm during an African
424 dust event. For a longer period of time (2005-2010), Valenzuela et al. (2012) computed
425 values of ARF and AFE with the radiative transfer model SBDART during African dust

events, and found ARF from -13 to -34 Wm^{-2} and AFE from -65 to $-74 \text{ Wm}^{-2}\tau^{-1}$ at 440 nm ,
 depending on the mineral sources. Foyo-Moreno et al. (2014), using the direct method
 for the radiative effects calculations, found an ARF of -28 Wm^{-2} and an AFE of $-73.4 \text{ Wm}^{-2}\tau^{-1}$
 at solar fixed angle of 15° during the period 2006-2007. Focusing on PAR Lyamani et
 al. (2006b) found values of ARF of $-20.4 \text{ Wm}^{-2}\tau^{-1}$ during an African dust event in 2003
 and -16.1 Wm^{-2} during intrusions from the Central Europe region, with AFE values of -73.4
 and $-78.2 \text{ Wm}^{-2}\tau^{-1}$ at 670 nm . Therefore, all these studies, performed in the same
 area of study, found values that are within the ranges of our findings. Other authors
 focused on other regions of the Mediterranean basin. Meloni et al. (2005), using a
 radiative transfer model at $400\text{-}700 \text{ nm}$, found ARF daily mean values -12.9 and -19.5
 Wm^{-2} in July and AFE at 500 nm ranging between -28.4 and $-30.1 \text{ Wm}^{-2}\tau^{-1}$ and between
 -42.9 and $-45.6 \text{ Wm}^{-2}\tau^{-1}$ for several days at Lampedusa. Sicard et al. (2016) for $50^\circ < \text{SZA}$
 $< 60^\circ$ found values of $\text{ARF}^{\text{total}}$ of $(-23 \pm 13) \text{ Wm}^{-2}$ and $(-136 \pm 41) \text{ Wm}^{-2}\tau^{-1}$ for $\text{AFE}^{\text{total}}$ in
 summer at Palma de Mallorca (Mallorca Island, Spain). All of these values are in good
 agreement with our findings.
 However, it is necessary to emphasize the different methodologies used in the works of
 most of the authors, deriving ARF from radiative transfer model calculation and
 obtaining averages daily values, whose calculations require aerosol information not
 known a priori. Thus, in a few cases instantaneous direct measurements of the net fluxes
 have been used to derive ARF, and further the effects of atmospheric aerosols on PAR
 scarcely have been studied.

4.3 Analysis of AFE and ARF trends

Figures 5b and 6b show the pattern followed for AFE and ARF, with an inflexion point at 60° for both PAR and Total irradiance, showing a similar pattern as described in section 4.2. This similar pattern is explained by the long path at high solar zenith angle, which includes strong attenuation of direct solar radiation but also more multiple scattering and hence more scattered light (Lyamani et al., 2006b). The dependence on SZA is more pronounced for ARF with respect to AFE. In spite of this growth pattern, values of AFE and ARF are close to be constant for angles smaller than 45° for both Total and PAR, and this finding are in agreement with previous studies for surface AFE estimated by radiative transfer model simulations (Formenti et al., 2002; Meloni et al., 2005). On the other hand, analyzing ARF^{PAR} and AFE^{PAR} by years, absolute terms, maximum values have been found in 2008 and 2009 (-10 Wm^{-2} , $-79 \text{ Wm}^{-2}\tau^{-1}$), and minimum values of -5.3 Wm^{-2} and $-41 \text{ Wm}^{-2}\tau^{-1}$ (ARF and AFE, respectively) both in 2015. For Total radiation maximum values are obtained in 2009 and 2018 (-22 Wm^{-2} and $-239 \text{ Wm}^{-2}\tau^{-1}$), and minimum values in 2015 (-12 Wm^{-2} and $-136 \text{ Wm}^{-2}\tau^{-1}$) (Figures 5a and 6a).

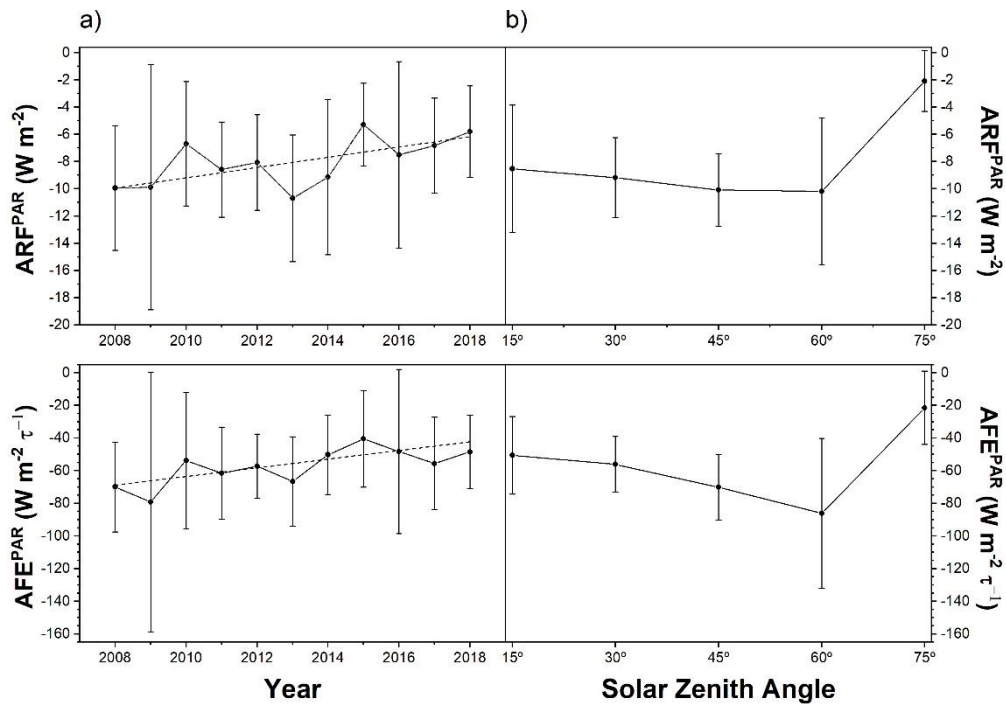


Figure 5. Evolution of surface aerosol radiative forcing for PAR (ARF^{PAR}) and surface aerosol forcing efficiency for PAR (AFE^{PAR}) with its variability at one standard deviation level by years and solar zenith angle (SZA). Dashed lines point out the linear trends evaluated by the Sen method.

The trends analyses revealed for ARF^{PAR} and AFE^{PAR} (considering absolute values) a downward trend for 2008-2018 period with a slope of $0.38 \text{ Wm}^{-2}\text{year}^{-1}$ and $2.66 \text{ Wm}^{-2}\tau^{-1}\text{year}^{-1}$, respectively, being significant for AFE with a p-value < 0.05 and very close to being significant for ARF (p-value = 0.062) (Figure 6a). Although the slope is positive, taking into account that the ARF (and AFE) values are negative, the slope value implies that the aerosol cooling radiative effect of aerosols is decreasing. The influence of calibration factor changes on this trend is negligible based on the long-term stability estimated for the PAR sensor along the analyzed period and described in Section 2. This result is interesting considering the decrease trend detected for AOD in the last years

already commented in section 4.1. However, no upward or downward trend has been observed for the annual evolution of ARF^{total} and AFE^{total} (Figure 6a). In order to consider a potential compensating effect of other spectral ranges, we have performed the calculation also with Total minus PAR, i.e. ultraviolet A and B plus near-infrared irradiance, and no statistically significant trend was found, although the slope is of opposite sign. This result can be attributed to aerosol properties especially to the aerosol absorption characteristics. In fact, AFE exhibits a dependence on single scattering albedo and a larger contribution of the PAR range in relation to Total irradiance is found for high absorbing aerosols (Mateos et al. 2014). These results indicate the importance of the knowledge of the PAR, because it is more sensitive to atmospheric aerosol effects than Total irradiance and, however, it has not been implemented nowadays at most radiometric stations instruments to measure routinely the PAR irradiance, unlike Total irradiance, which is a standard variable measured at the Baseline Surface Radiation Network (BSRN) and many other radiometric stations.

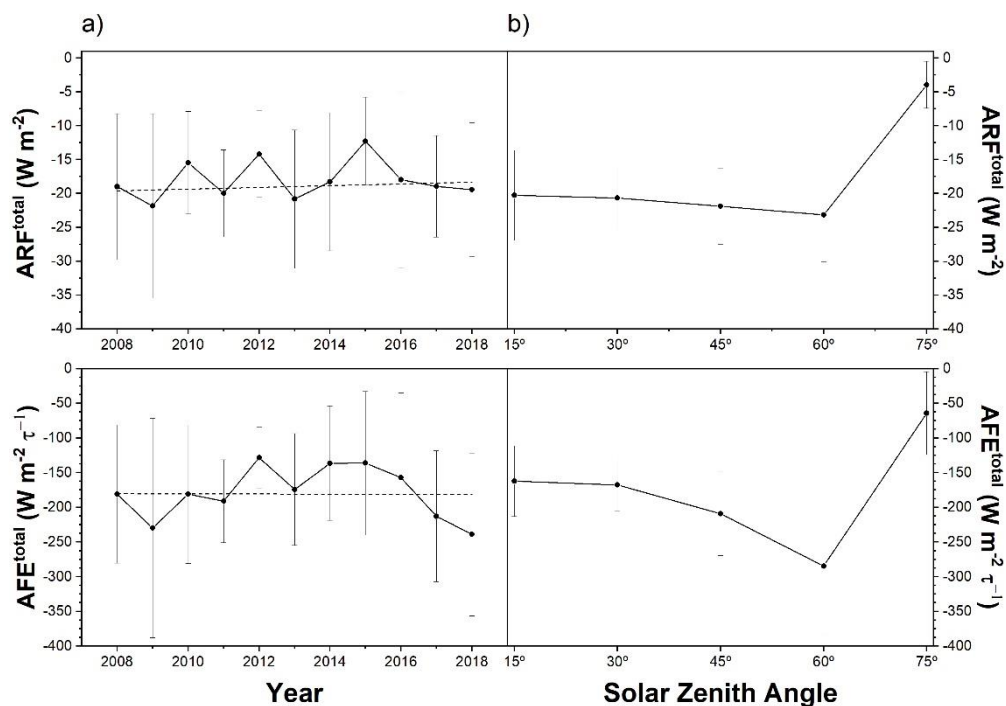


Figure 6. Evolution of surface aerosol radiative forcing for total irradiance (ARF^{total}) and surface aerosol forcing efficiency for total irradiance (AFE^{total}) with its variability at one standard deviation level by years and solar zenith angle (SZA). Dashed lines point out the linear trends evaluated by the Sen method.

5. CONCLUSIONS

Eleven years data set period were analyzed to determine the aerosols radiative effects in the photosynthetically active radiation (PAR; 400-700 nm) and Total irradiance (280-3000 nm) over an urban site located in a mid-latitude in the Western Mediterranean region. These effects have been analyzed through the estimation of aerosol forcing efficiency (AFE) and aerosol radiative forcing (ARF), using the direct method, obtaining instantaneous values from experimental measurements of aerosol optical depth (AOD)

and irradiance measurements. The advantage of this method unlike other methods using radiative model calculations is that it does not require aerosol information. The main conclusions are:

1. A seasonal evolution has been found with maximum AOD₅₀₀ values in summer (0.16 ± 0.09), corresponding to the highest incidence of Saharan dust events and minimum ones in winter (0.08 ± 0.04). The AFE values ranged between $(-12 \pm 9) \text{ Wm}^{-2}\tau^{-1}$ and $(-198 \pm 18) \text{ Wm}^{-2}\tau^{-1}$ for PAR while for Total the values varied from $(-9 \pm 24) \text{ Wm}^{-2}\tau^{-1}$ and $(-450 \pm 50) \text{ Wm}^{-2}\tau^{-1}$, meanwhile ARF values ranged from $(-1 \pm 1) \text{ Wm}^{-2}$ and $(-23 \pm 14) \text{ Wm}^{-2}$ in the case of PAR and from $(-1 \pm 2) \text{ Wm}^{-2}$ to $(-40 \pm 30) \text{ Wm}^{-2}$ for Total.
2. A dependence of both AFE and ARF on solar zenith angle was found with a clear pattern increasing values of ARF and AFE (in absolute sense) for increasing SZA, and an inflexion point at 45° - 60° range.
3. The percentage of ARF for PAR with respect to Total irradiance had a mean value of 50%, a higher value than that obtained for AFE (30%), evidencing the important impact of atmospheric aerosols on PAR because the ratio PAR/Total irradiance had a lower average value (43%).
4. A downward trend for AFE for PAR was found with a slope of $2.7 \text{ Wm}^{-2}\tau^{-1}\text{year}^{-1}$ with a p-value < 0.05 and no significative trend was found for Total irradiance, demonstrating that PAR is more sensitive to atmospheric aerosols effects than Total irradiance and, therefore, evidencing the need to increase the knowledge of PAR and its interaction with atmospheric aerosols.

5. The contribution of different spectral ranges in the trend analysis for AFE can be governed by the aerosol type, being in general, the visible spectral range the most dominant, with a variable contribution depending on the aerosol type.

ACKNOWLEDGMENTS This work was supported by the Spanish Ministry of Economy and Competitiveness through projects CGL2016-81092-R, CGL2017-90884-REDT and RTI2018.101154.A.I00, by the Andalusia Regional Government, University of Granada and FEDER funds through projects B-RNM-496-UGR18 and P18-RT-3820, and by the Spanish Ministry of Education, Culture and Sport through grant FPU15/05436. The financial support in the ACTRIS Research Infrastructure Project by the European Union's Horizon 2020 research and innovation program through project ACTRIS-2 (grant agreement No 654109) and ACTRIS-IMP (grant agreement No 871115). The authors thankfully acknowledge the FEDER program for the instrumentation used in this work and the University of Granada that supported this study through the Excellence Units Program.

REFERENCES

- Akitsu, T., Nasahara, K. N., Hirose, Y., Ijima, O., Kume, A., 2017. .Quantum sensors for accurate and stable long-term photosynthetically active radiation observations. Agr. For. Meteor., 237-238, 171-183. <https://doi.org/10.1016/j.agrformet.2017.01.011>
- Alados, I., Foyo-Moreno, I., Alados-Arboledas, L., 1996. Photosynthetically active radiation: Measurements and modelling. Agric. For. Meteor., 78, 121-131. [https://doi.org/10.1016/0168-1923\(95\)02245-7](https://doi.org/10.1016/0168-1923(95)02245-7).

553 Alados-Arboledas, L., Müller, D., Guerrero-Rascado, J. L., Navas-Guzmán, F., Pérez-
554 Ramírez, D., Olmo, F. J., 2011. Optical and microphysical properties of fresh biomass
555 burning aerosol retrieved by Raman lidar, and star-and sun-photometry. *J. Geophys.*
556 *Res. Letters*, 38. <https://doi.org/10.1029/2010GL045999>.

557 Alados-Arboledas, L., Olmo, F. J., Alados, I., Pérez, M., 2000. Parametric models to
558 estimate photosynthetically active radiation in Spain. *Agric. For. Meteorol.*, 101, 187-201.
559 [https://doi.org/10.1016/S0168-1923\(99\)00163-X](https://doi.org/10.1016/S0168-1923(99)00163-X).

560 Andreae, M. O., Jones, C. D., Cox, P. M., 2005. Strong present-day aerosol cooling implies
561 a hot future. *Nature*, 435, 1187–1190.

562 Antón, M., Gil, J. E., Fernández-Gálvez, J., Lyamani, H., Valenzuela, A., Foyo-Moreno, I.,
563 Olmo, F. J., Alados-Arboledas, L., 2011. Evaluation of the aerosol forcing efficiency in the
564 UV erythema range at Granada, Spain. *J. Geophys. Res.-Atmos.*, 116(D20), D20214.
565 <https://doi.org/10.1029/2011JD016112>.

566 Antón, M., Valenzuela, A., Cazorla, A., Gil, J. E., Fernández-Gálvez, J., Lyamani, H., Foyo-
567 Moreno, I., Olmo, F. J., Alados-Arboledas, L., 2012. Global and diffuse shortwave
568 irradiance during a strong desert dust episode at Granada (Spain). *Atmos. Res.*, 118, 232-
569 239. <https://doi.org/10.1016/j.atmosres.2012.07.007>.

570 Baars, H., Ansmann, A., Ohneiser, K., Haarig, M., Engelmann, R., Althausen, D., Hanssen,
571 I., Gausa, M., Pietruczuk, A., Szkop, A., Stachlewska, I. S., Wang, D., Reichardt, J., Skupin,
572 A., Mattis, I., Trickl, T., Vogelmann, H., Navas-Guzmán, F., Haefele, A., Pappalardo, G.,
573 2019. The unprecedented 2017-2018 stratospheric smoke event: Decay phase and
574 aerosol properties observed with the EARLINET. *Atmos. Chem. Phys.*, 19 (23), 15183-
575 15198. <https://doi.org/10.5194/acp-19-15183-2019>.

Benavent-Oltra, J. A., Román, R., Granados-Muñoz, M. J., Pérez-Ramírez, D., Ortiz-
Amezcu, P., Denjean, C., Lopatin, A., Lyamani, H., Torres, B., Guerrero-Rascado, J. L.,
Fuertes, D., Dubovik, O., Chaikovsky, A., Olmo, F. J., Mallet, M., Alados-Arboledas, L.,
2017. Comparative assessment of GRASP algorithm for a dust event over Granada
(Spain) during ChArMEx-ADRIMED 2013 campaign. *Atmos. Meas. Tech.*, *10*(11), 4439-
4457. <https://doi.org/10.5194/amt-10-4439-2017>.

Bennouna, Y.S., Cachorro, V.E. Mateos, D., Burgos, M.A., Toledano, C., Torres, B. , A.M.
de Frutos, A.M., 2016. Long-term comparative study of columnar and surface mass
concentration aerosol properties in a background environment. *Atmos. Env.*, *140*, 261-
272.

Bergstrom, R. W., Pilewskie, P., Russell, P. B., Redemann, J., Bond, T. C., Quinn, P. K.,
Sierau, B., 2007. Spectral absorption properties of atmospheric aerosols. *Atmos. Chem.
and Phys. Discuss.*, *7*(4), 10669-10686.

Bravo-Aranda, J. A., Titos, G., Granados-Muñoz, M. J., Guerrero-Rascado, J. L., Navas-
Guzmán, F., Valenzuela, A., Lyamani, H., Olmo, F. J., Andrey, J., Alados-Arboledas, L.,
2015. Study of mineral dust entrainment in the planetary boundary layer by lidar
depolarisation technique. *Tellus B: Chem. and Phys. Meteor.* *67*(1), 26180.
<https://doi.org/10.3402/tellusb.v67.26180>.

Buffoni, L., Maugeri, M., Nanni, T., 1999. Precipitation in Italy from 1833 to 1996. *Theo.
and App. Clim.*, *63* (1-2), 33–40.

Bush, B. C., Valero, F. P. J., 2003. Surface aerosol radiative forcing at Gosan during the
ACE-Asia campaign. *J. Geophys. Res. Atmos.*, *108* (D23).
<https://doi.org/10.1029/2002JD003233>.

599 Cariñanos, P., Foyo-Moreno, I., Alados, I., Juan Luis Guerrero-Rascado, J.L., Ruiz-Peñuela,
600 S., Titos, G., Cazorla A., Alados-Arboledas, L., Díaz de la Guardia, C., 2021. Bioaerosols in
601 urban environments: Trends and interactions with pollutants and meteorological
602 variables based on quasi-climatological series. *J. of Env. Manag.* 282, 111963.
603 <https://doi.org/10.1016/j.jenvman.2021.111963>.

604 Caya, M. V. C., Alcantara, J. T., Carlos, J. S., Cereno, S. S. B., 2018. Photosynthetically
605 active radiation (PAR) sensor using an array of light sensors with the integration of data
606 logging for agricultural application. *2018 3rd International Conference on Computer and*
607 *Communication Systems (ICCCS)*, 377–381.

608 Cazorla, A., Casquero-Vera, J. A., Román, R., Guerrero-Rascado, J. L., Toledano, C.,
609 Cachorro, V. E., Orza, J. A. G., Cancillo, M. L., Serrano, A., Titos, G., Pandolfi, M., Alastuey,
610 A., Hanrieder, N., Alados-Arboledas, L., 2017. Near-real-time processing of a ceilometer
611 network assisted with sun-photometer data: Monitoring a dust outbreak over the
612 Iberian Peninsula. *Atmos. Chem. and Phys.*, 17(19), 11861-11876.
613 <https://doi.org/10.5194/acp-17-11861-2017>.

614 Charlson, R. J., Langner, J., Rodhe, H., Leovy, C. B., Warren, S. G., 1991. Perturbation of
615 the northern hemisphere radiative balance by backscattering from anthropogenic
616 sulfate aerosols. *Tellus A: Dynamic Meteorol. and Oceano.*, 43(4), 152–163.

617 Córdoba-Jabonero, C., Sorribas, M., Guerrero-Rascado, J. L., Adame, J. A., Hernández, Y.,
618 Lyamani, H., Cachorro, V., Gil, M., Alados-Arboledas, L., Cuevas, E., de la Morena, B.,
619 2011. Synergetic monitoring of Saharan dust plumes and potential impact on surface: A
620 case study of dust transport from Canary Islands to Iberian Peninsula. *Atmos. Chem. and*
621 *Phys.*, 11(7), 3067-3091. <https://doi.org/10.5194/acp-11-3067-2011>.

Da Silva, V. de P. R., e Silva, R. A., Cavalcanti, E. P., Braga, C. C., de Azevedo, P. V., Singh, V. P., Pereira, E. R. R., 2010. Trends in solar radiation in NCEP/NCAR database and measurements in northeastern Brazil. *Sol. Energ.*, 84(10), 1852–1862.

Dadashi-Roudbari, A., Ahmadi, M., 2020. Evaluating temporal and spatial variability and trend of aerosol optical depth (550 nm) over Iran using data from MODIS on board the Terra and Aqua satellites. *Arabian J. of Geosciences*, 13(6), 1-23. <https://doi.org/10.1007/s12517-020-5232-0>.

Di Biagio, C., di Sarra, A., Meloni, D., 2010. Large atmospheric shortwave radiative forcing by Mediterranean aerosols derived from simultaneous ground-based and spaceborne observations and dependence on the aerosol type and single scattering albedo. *J. of Geophys. Res.*, 115 (D10), D10209. <https://doi.org/10.1029/2009JD012697>.

Di Biagio, C., di Sarra, A., Meloni, D., Monteleone, F., Piacentino, S., Sferlazzo, D., 2009. Measurements of Mediterranean aerosol radiative forcing and influence of the single scattering albedo. *J. Geophys. Res.*, 114(D6), D06211. <https://doi.org/10.1029/2008JD011037>.

Díaz, A. M., García, O. E., Díaz, J. P., Expósito, F. J., Utrillas, M. P., Martínez-Lozano, J. A., Alados-Arboledas, L., Olmo, F. J., Lorente, J., Cachorro, V., Horvath, H., Labajo, A., Sorribas, M., Vilaplana, J. M., Silva, A. M., Elias, T., Pujadas, M., Rodrigues, J. A., González, J. A., 2007. Aerosol radiative forcing efficiency in the UV region over southeastern Mediterranean: VELETA2002 campaign. *J. Geophys. Res.*, 112(D6), D06213. <https://doi.org/10.1029/2006JD007348>.

Esteve, A. R., Estellés, V., Utrillas, M. P., Martínez-Lozano, J. A., 2012. In-situ integrating nephelometer measurements of the scattering properties of atmospheric aerosols at an urban coastal site in western Mediterranean. *Atmos. Environ.*, 47, 43–50.

Eswaran, K., Satheesh, S. K., Srinivasan, J., 2019. Sensitivity of aerosol radiative forcing to various aerosol parameters over the Bay of Bengal. *J. of Earth System Scien.*, 128 (6), 170. <https://doi.org/10.1007/s12040-019-1200-z>.

Farahat, A., El-Askary, H., Adetokunbo, P., Fuad, A.T., 2016. Analysis of aerosol absorption properties and transport over North Africa and the Middle East using AERONET data. *Ann. Geophys.*, 34(11), 1031-1044. <https://doi.org/10.5194/angeo-34-1031-2016>.

Fernández, A. J., Sicard, M., Costa, M. J., Guerrero-Rascado, J. L., Gómez-Amo, J. L., Molero, F., Barragán, R., Basart, S., Bortoli, D., Bedoya-Velásquez, A. E., 2019. Extreme wintertime Saharan dust intrusion in the Iberian Peninsula: Lidar monitoring and evaluation of dust forecast models during the February 2017 event. *Atmos. Res.*, 228, 223–241.

Formenti, P., Boucher, O., Reiner, T., Sprung, D., Andreae, M. O., Wendisch, M., Wex, H., Kindred, D., Tzortziou, M., Vasaras, A., Zerefos, C., 2002. STAAARTE-MED 1998 summer airborne measurements over the Aegean Sea 2. Aerosol scattering and absorption, and radiative calculations. *J. Geophys. Res. Atmos.*, 107(D21), AAC 2-1-AAC 2-14. <https://doi.org/10.1029/2001JD001536>.

Foyo-Moreno, I., Alados, I., Alados-Arboledas, L., 2017. A new conventional regression model to estimate hourly photosynthetic photon flux density under all sky conditions: *Int. J. Clim.*, 37, 1067-1075. <https://doi.org/10.1002/joc.5063>.

Foyo-Moreno, I., Alados, I., Antón, M., Fernández-Gálvez, J., Cazorla, A., Alados-Arboledas, L., 2014. Estimating aerosol characteristics from solar irradiance measurements at an urban location in southeastern Spain: Aerosol properties from solar irradiance. *J. Geophys. Res. Atmos.*, 119(4), 1845-1859. <https://doi.org/10.1002/2013JD020599>.

Foyo-Moreno, I., Alados, I., Guerrero-Rascado, J. L., Lyamani, H., Pérez-Ramírez, D., Olmo, F. J., Alados-Arboledas, L., 2019. Contribution to column-integrated aerosol typing based on Sun-photometry using different criteria. *Atmos. Res.*, 224, 1–17. <https://doi.org/10.1016/j.atmosres.2019.03.007>.

García, O. E., Díaz, A. M., Expósito, F. J., Díaz, J. P., Gröbner, J., Fioletov, V. E., 2006. Cloudless aerosol forcing efficiency in the UV region from AERONET and WOUDC databases. *Geophys. Res. Lett.*, 33(23), L23803. <https://doi.org/10.1029/2006GL026794>.

Garcia-Herrera, R. F., Lionello, P., Ulbrich, U., 2014. Preface: Understanding dynamics and current developments of climate extremes in the Mediterranean region. *Nat. Hazards Earth Syst. Sci.*, 8.

Ge, S., Smith, R. G., Jacovides, C. P., Kramer, M. G., Carruthers, R. I., 2011. Dynamics of photosynthetic photon flux density (PPFD) and estimates in coastal northern California. *Theor. App. Clim.*, 105(1-2), 107-118. <https://doi.org/10.1007/s00704-010-0368-6>.

Giles, D. M., Sinyuk, A., Sorokin, M. G., Schafer, J. S., Smirnov, A., Slutsker, I., Eck, T. F., Holben, B. N., Lewis, J. R., Campbell, J. R., Welton, E. J., Korkin, S. V., Lyapustin, A. I., 2019. Advancements in the Aerosol Robotic Network (AERONET) Version 3 database – automated near-real-time quality control algorithm with improved cloud screening for <https://doi.org/10.1016/j.atmosres.2021.105538>

Sun photometer aerosol optical depth (AOD) measurements. *Atmos. Meas. Tech.*, 12(1), 169-209. <https://doi.org/10.5194/amt-12-169-2019>.

Gkikas, A., Hatzianastassiou, N., Mihalopoulos, N., Katsoulis, V., Kazadzis, S., Pey, J., Querol, X., Torres, O., 2013. The regime of intense desert dust episodes in the Mediterranean based on contemporary satellite observations and ground measurements. *Atmos. Chem. and Phys.*, 13(23), 12135-12154. <https://doi.org/10.5194/acp-13-12135-2013>.

Gkikas, A., Obiso, V., Pérez García-Pando, C., Jorba, O., Hatzianastassiou, N., Vendrell, L., Basart, S., Solomos, S., Gassó, S., Baldasano, J. M., 2018. Direct radiative effects during intense Mediterranean desert dust outbreaks. *Atmos. Chem. and Phys.*, 18(12), 8757-8787. <https://doi.org/10.5194/acp-18-8757-2018>.

Gopal, K. R., Arafath, S. M., Lingaswamy, A. P., Balakrishnaiah, G., Kumari, S. P., Devi, K. U., Reddy, N. S. K., Reddy, K. R. O., Reddy, M. P., Reddy, R. R., 2014. In-situ measurements of atmospheric aerosols by using Integrating Nephelometer over a semi-arid station, southern India. *Atmos. Env.*, 86, 228–240.

Granados-Muñoz, M. J., Sicard, M., Román, R., Benavent-Oltra, J. A., Barragán, R., Brogniez, G., Denjean, C., Mallet, M., Formenti, P., Torres, B., 2019. Impact of mineral dust on shortwave and longwave radiation: Evaluation of different vertically resolved parameterizations in 1-D radiative transfer computations. *Atmos. Chem. and Phys.*, 19(1), 523–542. <https://doi.org/10.5194/acp-19-523-2019>.

Guerrero-Rascado, J. L., Olmo, F. J., Avilés-Rodríguez, I., Navas-Guzmán, F., Pérez-Ramírez, D., Lyamani, H., Alados Arboledas, L., 2009. Extreme Saharan dust event over the southern Iberian Peninsula in september 2007: Active and passive remote sensing

from surface and satellite. *Atmos. Chem. and Phys.*, 9(21), 8453-8469.
<https://doi.org/10.5194/acp-9-8453-2009>.

Guerrero-Rascado, J. L., Ruiz, B., Alados-Arboledas, L., 2008. Multi-spectral Lidar characterization of the vertical structure of Saharan dust aerosol over southern Spain. *Atmos. Env.*, 42(11), 2668-2681. <https://doi.org/10.1016/j.atmosenv.2007.12.062>

Hansen, J., Sato, M., Kharecha, P., Von Schuckmann, K., 2011. Earth's energy imbalance and implications. *Atmos. Chem. and Phys.*, 11(24), 13421-13449.
<https://doi.org/10.5194/acp-11-13421-2011>.

Holben, B. N., Eck, T. F., Slutsker, I., Tanré, D., Buis, J. P., Setzer, A., Vermote, E., Reagan, J. A., Kaufman, Y. J., Nakajima, T., Lavenu, F., Jankowiak, I., Smirnov, A., 1998. AERONET—A Federated Instrument Network and Data Archive for Aerosol Characterization. *Rem. Sens. of Env.*, 66(1), 1-16. [https://doi.org/10.1016/S0034-4257\(98\)00031-5](https://doi.org/10.1016/S0034-4257(98)00031-5).

Iqbal, M. 1983. *An Introduction to Solar Radiation*. Academic Press: London.

Jeff Burkey., 2020. Mann-Kendall Tau-b with Sen's Method (enhanced) (<https://www.mathworks.com/matlabcentral/fileexchange/11190-mann-kendall-tau-b-with-sen-s-method-enhanced>), MATLAB Central File Exchange. Retrieved December 23, 2020 <https://www.mathworks.com/matlabcentral/fileexchange/11190-mann-kendall-tau-b-with-sen-s-method-enhanced>.

Jonard, F., De Cannière, S., Brüggemann, N., Gentine, P., Short Gianotti, D. J., Lobet, G., Miralles, D. G., Montzka, C., Pagán, B. R., Rascher, U., Vereecken, H., 2020. Value of sun-induced chlorophyll fluorescence for quantifying hydrological states and fluxes: Current

734 status and challenges. *Agr. and For. Meteorol.*, 291, 108088.
735 <https://doi.org/10.1016/j.agrformet.2020.108088>.

736 Kodera, K., Hori, M. E., Yukimoto, S., Sigmond, M., 2008. Solar modulation of the
737 Northern Hemisphere winter trends and its implications with increasing CO₂. *Geophys.*
738 *Research Letters*, 35(3).

739 Kuo, C.-C., Gan, T. Y., Wang, J., 2020. Climate change impact to Mackenzie river Basin
740 projected by a regional climate model. *Clim. Dyn.*, 54(7), 3561-3581.
741 <https://doi.org/10.1007/s00382-020-05177-7>.

742 Li, L., Li, Z., Chang, W., Ou, Y., Goloub, P., Li, C., Li, K., Hu, Q., Wang, J., Wendisch, M.
743 2020. Aerosol solar radiative forcing near the Taklimakan Desert based on radiative
744 transfer and regional meteorological simulations during the Dust Aerosol Observation-
745 Kashi campaign. *Atmos. Chem. and Phys.*, 20(18), 10845-10864.
746 <https://doi.org/10.5194/acp-20-10845-2020>.

747 Lionello, P., Abrantes, F., Gacic, M., Planton, S., Trigo, R., Ulbrich, U., 2014. The climate
748 of the Mediterranean region: Research progress and climate change impacts. *Reg. Env.*
749 *Change*, 14(5), 1679-1684. <https://doi.org/10.1007/s10113-014-0666-0>.

750 Lyamani, H., Fernandez-Galvez, J., Perez-Ramirez, D., Valenzuela, A., Anton, M., Alados,
751 I., Titos, G., Olmo, F. J., Alados-Arboledas, L., 2012. Aerosol properties over two urban
752 sites in South Spain during an extended stagnation episode in winter season. *Atmos.*
753 *Env.*, 62, 424-432. <https://doi.org/10.1016/j.atmosenv.2012.08.050>.

Lyamani, H., Olmo, F. J., Alados-Arboledas, L., 2010. Physical and optical properties of aerosols over an urban location in Spain: Seasonal and diurnal variability. *Atmos. Chem. and Phys.*, 10, 239-254.

Lyamani, H., Olmo, F. J., Alcántara, A., Alados-Arboledas, L., 2006a. Atmospheric aerosols during the 2003 heat wave in southeastern Spain I: Spectral optical depth. *Atmos. Env.*, 40(33), 6453-6464. <https://doi.org/10.1016/j.atmosenv.2006.04.048>.

Lyamani, H., Olmo, F. J., Alcántara, A., Alados-Arboledas, L., 2006b. Atmospheric aerosols during the 2003 heat wave in southeastern Spain II: Microphysical columnar properties and radiative forcing. *Atmos. Env.*, 40(33), 6465-6476. <https://doi.org/10.1016/j.atmosenv.2006.04.047>.

Ma, J., Liu, J., Li, S., Liang, H., Jiang, C. Y., Wang, B. Z., 2007. Study on the features of the photosynthetic active radiation (PAR) with experimentations and measurements. *J. of Nat. Resources*, 22 (5), 673-682. <http://dx.doi.org/10.11849/zrzyxb.2007.05.001>.

Mann, H. B. 1945. Nonparametric Tests Against Trend. *Econometrica*, 13(3), 245-259. JSTOR. <https://doi.org/10.2307/1907187>.

Li, J., Carlson, B.E., Dubovik, O., Lacis, A.A., 2014. Recent trends in aerosol optical properties derived from AERONET measurements. *Atmos. Chem. Phys.* 14, 12271–12289. <http://dx.doi.org/10.5194/acp-14-12271-2014>.

Mateos, D., Antón, M., Toledano, C., Cachorro, V. E., Alados-Arboledas, L., Sorribas, M., Costa, M. J., Baldasano, J. M., 2014. Aerosol radiative effects in the ultraviolet, visible, and near-infrared spectral ranges using long-term aerosol data series over the Iberian

775 Peninsula. Atmos. Chem. and Phys., 14(24), 13497-13514. [https://doi.org/10.5194/acp-](https://doi.org/10.5194/acp-14-13497-2014)
776 [14-13497-2014](https://doi.org/10.5194/acp-14-13497-2014).

777 Mateos, D., Cachorro, V. E., Toledano, C., Burgos, M.A., Bennouna, Y., Torres, B., Fuertes,
778 D., Gonzalez, R., Guirado, C., Calle, A., de Frutos., 2015. Columnar and surface aerosol
779 load over the Iberian Peninsula establishing annual cycles, trends, and relationships in
780 five geographical sectors. The Scien. of the Total Env., 518-519, 378-392.

781 McCree, K. J., 1972. Test of current definitions of photosynthetically active radiation
782 against leaf photosynthesis data. Agr. Meteor., 10, 443-453.
783 [https://doi.org/10.1016/0002-1571\(72\)90045-3](https://doi.org/10.1016/0002-1571(72)90045-3).

784 McCree, K. J., 1981. Photosynthetically Active Radiation. En O. L. Lange, P. S. Nobel, C.
785 B. Osmond, & H. Ziegler (Eds.), Physiological Plant Ecology I (pp. 41-55). Springer Berlin
786 Heidelberg. https://doi.org/10.1007/978-3-642-68090-8_3.

787 Meloni, D., di Sarra, A., Di Iorio, T., Fiocco, G., 2005. Influence of the vertical profile of
788 Saharan dust on the visible direct radiative forcing. J- of Quantitative Spectroscopy and
789 Rad. Transfer, 93(4), 397-413. <https://doi.org/10.1016/j.jqsrt.2004.08.035>.

790 Nabat, P., Somot, S., Mallet, M., Sevault, F., Marc Chiacchio, M., Wild, M., 2015. Direct
791 and semi-direct aerosol radiative effect on the Mediterranean climate variability using
792 a coupled regional climate system model. Clym. Dyn., 44, 1127-1155.

793 Navas-Guzmán, F., Müller, D., Bravo-Aranda, J. A., Guerrero-Rascado, J. L., Granados-
794 Muñoz, M. J., Pérez-Ramírez, D., Olmo, F. J., Alados-Arboledas, L., 2013. Eruption of the
795 Eyjafjallajökull Volcano in spring 2010: Multiwavelength Raman lidar measurements of

796 sulphate particles in the lower troposphere. *J. of Geophys. Res.: Atmos.*, *118*(4), 1804-
797 1813. <https://doi.org/10.1002/jgrd.50116>.

798 Nemasure, S., Wagener, R., Schwartz, S. E., 1995. Direct shortwave forcing of climate by
799 the anthropogenic sulfate aerosol: Sensitivity to particle size, composition, and relative
800 humidity. *J. of Geophys. Res.*, *100*(D12), 26,105-26,116. Scopus.
801 <https://doi.org/10.1029/95jd02897>.

802 Obregón, M. A., Costa, M.J.; Serrano, A., Silva A.M., 2017. A. Thirteen Years of Aerosol
803 Radiative Forcing in Southwestern Iberian Peninsula. *Aerosol Air Qual. Res.* 2017, *17*,
804 2509–2521.

805 Obregón, M. A., Costa, M.J.; Silva A.M.; Serrano, A., 2020. Spatial and Temporal Variation
806 of Aerosol and Water Vapour Effects on Solar Radiation in the Mediterranean Basin
807 during the Last Two Decades. *Remote Sens.*, *12*, 1316; <https://doi:10.3390/rs12081316>.

808 Olmo, F. J., Alados-Arboledas, L., 1995. Pinatubo eruption effects on solar radiation at
809 Almeria (36.83 N, 2.41 W). *Tellus B: Chem. and Phys. Meteorol.*, *47*(5), 602–606.

810 Ortiz-Amezcu, P., Guerrero-Rascado, J. L., Granados-Muñoz, M. J., Bravo-Aranda, J. A.,
811 Alados-Arboledas, L., 2014. Characterization of atmospheric aerosols for a long range
812 transport of biomass burning particles from canadian forest fires over the southern
813 iberian peninsula in July 2013. *Óptica Pura y Aplicada*, *47*(1), 43–49.

814 Ortiz-Amezcu, P., Guerrero-Rascado, J. L., Granados-Muñoz, M. J., Benavent-Oltra, J.
815 A., Böckmann, C., Samaras, S., Stachlewska, I. S., Janicka, Ł., Baars, H., Bohlmann, S.,
816 Alados-Arboledas, L., 2017. Microphysical characterization of long-range transported

biomass burning particles from North America at three EARLINET stations. *Atmos. Chem. and Phys.*, 17(9), 5931-5946. <https://doi.org/10.5194/acp-17-5931-2017>.

Pérez-Ramírez, D., Lyamani, H., Smirnov, A., O'Neill, N. T., Veselovskii, I., Whiteman, D. N., Olmo, F. J., Alados-Arboledas, L., 2016. Statistical study of day and night hourly patterns of columnar aerosol properties using sun and star photometry. *Rem. Sens. of Clouds and the Atmos. XXI*, 10001, 100010K. <https://doi.org/10.1117/12.2242372>.

Potter, C., Boriah, S., Steinbach, M., Kumar, V., Klooster, S., 2007. Terrestrial vegetation dynamics and global climate controls. *Clim. Dynamics*, 31(1), 67–78.

Potter, C., Boriah, S., Steinbach, M., Kumar, V., Klooster, S., 2008. Terrestrial vegetation dynamics and global climate controls in North America: 2001–05. *Earth Interactions*, 12(8), 1–12.

Querol, X., Pey, J., Pandolfi, M., Alastuey, A., Cusack, M., Pérez, N., Moreno, T., Viana, M., Mihalopoulos, N., Kallos, G., Kleanthous, S., 2009. African dust contributions to mean ambient PM₁₀ mass-levels across the Mediterranean Basin. *Atmos. Env.*, 43(28), 4266-4277. <https://doi.org/10.1016/j.atmosenv.2009.06.013>.

Romano, S., Burlizzi, P., Perrone, M. R., 2016. Experimental determination of short- and long-wave dust radiative effects in the Central Mediterranean and comparison with model results. *Atmos. Res.*, 171, 5-20. <https://doi.org/10.1016/j.atmosres.2015.11.019>.

Salvador, P., Alonso-Pérez, S., Pey, J., Artíñano, B., de Bustos, J. J., Alastuey, A., Querol, X., 2014. African dust outbreaks over the western Mediterranean Basin: 11-year characterization of atmospheric circulation patterns and dust source areas. *Atmos. Chem. and Phys.*, 14(13), 6759-6775. <https://doi.org/10.5194/acp-14-6759-2014>.

839 Satheesh, S. K., Krishna Moorthy, K., 2005. Radiative effects of natural aerosols: A
840 review. Atmos. Env., 39(11), 2089-2110.
841 <https://doi.org/10.1016/j.atmosenv.2004.12.029>.

842 Satheesh, S. K., Ramanathan, V., 2000. Large differences in tropical aerosol forcing at
843 the top of the atmosphere and Earth's surface. Nature, 405(6782), 60-63.
844 <https://doi.org/10.1038/35011039>.

845 S. Segura, S., Estelles, V., Utrillas, M.P., Martínez-Lozano, J.A., 2017. Long term analysis
846 of the columnar and surface aerosol relationship at an urban European coastal site.
847 Atmos. En., 167, 309-322. <https://dx.doi.org/10.1016/j.atmosenv.2017.08.012>.

848 Sen, P. K., 1968. Estimates of the regression coefficient based on Kendall's tau. J. of the
849 American statistical association, 63(324), 1379-1389.

850 Sicard, M., Guerrero-Rascado, J. L., Navas-Guzmán, F., Preißler, J., Molero, F., Torrés, S.,
851 Bravo-Aranda, J. A., Comerón, A., Rocadenbosch, F., Wagner, F., Pujadas, M., Alados-
852 Arboledas, L., 2012. Monitoring of the Eyjafjallajökull volcanic aerosol plume over the
853 Iberian Peninsula by means of four EARLINET lidar stations. Atmos. Chem. and Phys.,
854 12(6), 3115-3130. <https://doi.org/10.5194/acp-12-3115-2012>.

855 Sicard, M., Barragan, R., Dulac, F., Alados-Arboledas, L., Mallet, M., 2016. Aerosol
856 optical, microphysical and radiative properties at regional background insular sites in
857 the western Mediterranean. Atmos. Chem. Phys., 16, 12177-12203.
858 <https://doi.org/10.5194/acp-16-12177-2016>.

859 Sivan, C., Manoj, M. G., 2019. Aerosol and cloud radiative forcing over various hot spot
860 regions in India. *Advances in Space Res.*, 64(8), 1577-1591.
861 <https://doi.org/10.1016/j.asr.2019.07.028>.

862 Sorribas, M., Andrews, E., Ogren, J. A., del Águila, A., Fraile, R., Sheridan, P., Yela, M. ,
863 2019. Climatological study for understanding the aerosol radiative effects at southwest
864 Atlantic coast of Europe. *Atmos. Env.*, 205, 52-66.
865 <https://doi.org/10.1016/j.atmosenv.2019.02.017>.

866 Stocker, T. F., Qin, D., Plattner, G. K., Tignor, M., Allen, S. K., Boschung, J., Nauels, A., Xia,
867 Y., Bex, V., Midgley, P. M., 2013. IPCC, 2013. *Climate Change*.

868 Titos, G., Del Águila, A., Cazorla, A., Lyamani, H., Casquero-Vera, J. A., Colombi, C.,
869 Cuccia, E., Gianelle, V., Močnik, G., Alastuey, A., Olmo, F. J., Alados-Arboledas, L., 2017.
870 Spatial and temporal variability of carbonaceous aerosols: Assessing the impact of
871 biomass burning in the urban environment. *The Sci. of the Total Env.*, 578, 613-625.
872 <https://doi.org/10.1016/j.scitotenv.2016.11.007>.

873 Titos, G., Foyo-Moreno, I., Lyamani, H., Querol, X., Alastuey, A., Alados-Arboledas, L.,
874 2012. Optical properties and chemical composition of aerosol particles at an urban
875 location: An estimation of the aerosol mass scattering and absorption efficiencies. *J. of*
876 *Geophys. Res.: Atmos.*, 117(D4).

877 Valenzuela, A., Olmo Reyes, F. J., Lyamani, H., Antón, M., Quirantes Sierra, A., Alados-
878 Arboledas, L., 2012. Aerosol radiative forcing during African desert dust events (2005–
879 2010) over Southeastern Spain. *Atmos. Chem. Phys. Discuss.*, 12, 6593–6622.

Wu, B.-S., Rufyikiri, A.-S., Orsat, V., Lefsrud, M. G., 2019. Re-interpreting the photosynthetically action radiation (PAR) curve in plants. *Plant Science*, 289, 110272. <https://doi.org/10.1016/j.plantsci.2019.110272>.

Xu, J., Bergin, M. H., Greenwald, R., Russell, P. B., 2003. Direct aerosol radiative forcing in the Yangtze delta region of China: Observation and model estimation. *J. of Geophys. Res.: Atmos.*, 108(D2). <https://doi.org/10.1029/2002JD002550>.

Zhang, M., Wang, Y., Ma, Y., Wang, L., Gong, W., Liu, B., 2018. Spatial distribution and temporal variation of aerosol optical depth and radiative effect in South China and its adjacent area. *Atmos. Env.*, 188, 120-128. <https://doi.org/10.1016/j.atmosenv.2018.06.028>.

Zhu, Z., Wang, L., Gong, W., Xiong, Y., Hu, B., 2015. Observation and estimation of photosynthetic photon flux density in Southern China. *Theor. and App. Clim.*, 120(3-4), 701-712. <https://doi.org/10.1007/s00704-014-1204-1>.

Zhuang, B. L., Li, S., Wang, T. J., Deng, J. J., Xie, M., Yin, C. Q., Zhu, J. L., 2013. Direct radiative forcing and climate effects of anthropogenic aerosols with different mixing states over China. *Atmos. Env.*, 79, 349–361.

Zou, L., Lin, A., Wang, L., Xia, X., Gong, W., Zhu, H., Zhao, Z., 2016. Long-term variations of estimated global solar radiation and the influencing factors in Hunan province, China during 1980–2013. *Meteorol. and Atmos. Phys.*, 128(2), 155–165.